Geophysical Journal International
September 2012, Vol. 190, Issue 3, pages 1746–1760
http://dx.doi.org/10.1111/j.1365-246X.2012.05601.x

Multiscale seismic attributes: source-corrected wavelet response and application to high-resolution seismic data

Stephan Ker[1, 2, *], Yves Le Gonidec[3], Dominique Gibert[2]

[1] IFREMER, Département Géosciences marines, Centre de Brest, 29280 Plouzané, France
[2] Institut de Physique du Globe de Paris (CNRS UMR 7154), Sorbonne Paris Cité, 1 rue Jussieu, 75238 Paris cedex, France
[3] Géosciences Rennes (CNRS UMR 6118), Université Rennes 1, Bât. 15 Campus de Beaulieu, 35042 Rennes cedex, France

*: Corresponding author : S. Ker, email address : stephan.ker@ifremer.fr

Abstract:

A wavelet-based method was presented in a previous work to introduce multiscale seismic attributes for high-resolution seismic data. Because of the limited frequency bandwidth of the seismic source, we observed distortions in the seismic attributes based on the wavelet response of the subsurface discontinuities (Le Gonidec *et al.*). In this paper, we go further in the seismic source-correction by considering Lévy alpha-stable distributions introduced in the formalism of the continuous wavelet transform (CWT). The wavelets are Gaussian derivative functions (GDF), characterized by a derivative order. We show that a high-resolution seismic source, after a classical signature processing, can be taken into account with a GDF. We demonstrate that in the framework of the Born approximation, the CWT of a seismic trace involving such a finite frequency bandwidth can be made equivalent to the CWT of the impulse response of the subsurface and is defined for a reduced range of dilations. We apply the method for the SYSIF seismic device (Marsset *et al.*; Ker *et al.*) and show that the source-corrections allow to define seismic attributes for layer thicknesses in the range [24; 115 cm]. We present the analysis for two seismic reflectors identified on a SYSIF profile, and we show that the source-corrected multiscale analysis quantifies their complex geometries.

Keywords: Wavelet transform; Wave propagation; Acoustic properties

1 INTRODUCTION

The geophysical characterization of marine sediments over large areas is generally greatly improved when seismic data are joined with local ground truth measurements providing information on the physical properties of the geological materials constituting the subseabed (e.g. Sherrif, 1992; Pennington, 2001; Sultan et al., 2007). This joined interpretation extensively uses various seismic attributes from which the interpreters derive quantitative relations between attributes and sediments properties (Fomel, 2007; Barnes, 2001; Gastaldi et al., 1997). Such interpretations are faced with a noticeable difficulty when relating seismic attributes to in situ measurements because of the huge discrepancy in the scale ranges associated with both kind of data, i.e. seismic wavelengths and layer thickness ranges (Widess, 1973; Morlet et al., 1982; Banik et al., 1985; Burridge et al., 1988). Recent technological improvements of seismic devices result in a significant extension of the frequency range available toward the high-frequencies (Wood et al., 2003; Marsset et al., 2010; Ker et al., 2010). The availability of seismic data spanning several octaves of wavelengths motivates developments of analysis methods relying on the multiscale analysis of seismic traces such as the windowed Fourier transform and the wavelet transform (Le Gonidec et al., 2002; Castagna et al., 2003; Chopra et al., 2006, Gesret et al., 2010; Ker et al., 2011). Introduced by Le Gonidec et al. (2002), the wavelet response (WR) is a promising method to perform a multiscale characterization of complex discontinuities. Assuming the validity of the Born approximation, the authors demonstrate that the wavelet response (WR) is equivalent to the continuous wavelet transform (CWT), i.e. the analysis from the WR benefit by the properties of the CWT. In particular, the method has already been experimented to study granular interfaces from the analysis of the ridge functions (Le Gonidec et al., 2006; Le Gonidec et al., 2007). Remarkably, all information necessary to characterize the discontinuities forming the reflector is brought by the ridge functions connecting the extrema of the wavelet transform and forming a sparse support (Mallat & Hwang, 1992; Alexandrescu et al. 1995; Mallat, 1998; Le Gonidec et al. 2002).
For laboratory studies in acoustics, Le Gonidec et al. (2002, 2003) uses a family of dilated wavelets as source signals to record the experimental WR of random media. The wavelet based method contributes efficiently to the understanding of the wavelet decomposition ofreflected signals by exploit-

ing wave propagation phenomena. From this point of view, the WR represents the collection of traces which would be obtained by sounding the medium with an ensemble of wavelet signals forming a wavelet family. However, such an ideal approach is not possible when dealing with general source signals, i.e. the limited frequency band of such sources should produce distortions of the ridge functions. Indeed, the first time the WR method has been performed to seismic data by using the ridge functions as new multiscale seismic attributes, strong distortions of the ridge function were clearly observed (Ker *et al.*, 2011).

To go further into this original multiscale seismic analysis, recalled in Section 2, the present paper aims at fully correcting the ridge functions according to the specific processing method described in Section 3. The method is based on the properties of Lévy alpha-stable distributions $L(t)$ (Voit, 2003) and we show that effective analysing wavelets, required for the source-corrected wavelet response, may be obtained if both the analysing wavelet $\xi(t)$ and the source filter $b(t)$ are derivatives of $L(t)$. Section 4 is dedicated to determine the Gaussian wavelet model for a real seismic source so as to apply the mathematical development to seismic experiments. In Section 5, the methodology is applied to the deep-towed seismic SYSIF sources. We discuss the dilation range of the best gaussian filters related to the band-limited seismic sources to perform the source-corrected wavelet response of a thin homogeneous layer. In the last section, we process real field data according to this approach and we demonstrate and discuss the validity of the method on complex seismic traces.

2 REMINDER OF THE WAVELET-BASED METHOD

In a previous paper (Ker *et al.*, 2011), we propose a wavelet transform approach to perform a multiscale characterization of acoustic impedance discontinuities from seismic data. This method contributes to the understanding of the wavelet decomposition of seismic signals by exploiting wave propagation phenomena and it is based on the wavelet response (WR) introduced by Le Gonidec *et al.* (2002). The wavelet response is a natural extension of the classical continuous wavelet transform (CWT) where the convolution operator is replaced by the propagating operator involved by seismic waves. The WR is expressed by:

$$R\left[\xi, p\right](t,a) \equiv \left(\mathcal{D}_a\xi \otimes p\right)(t) \tag{1a}$$

$$= \mathcal{D}_a\xi(t) * r(t) \tag{1b}$$

$$= W\left[\xi, r\right](t,a)\,, \tag{1c}$$

where ξ is the analysing wavelet and $\mathcal{D}_a$ is the dilation operator such that $\mathcal{D}_a\xi\left(t\right) = a^{-1}\xi(t/a)$ with the dilation factor $a \in \mathbb{R}^+$. The operator $\otimes$ represents the 1-D propagation of the wavelet fam-

ily through the medium with impedance $p(z)$, and $*$ stands for convolution. The introduction of the Green's function of the medium $r(t)$ instead of $p(z)$ allows to write the wavelet response R as the wavelet transform W of $r(t)$ in eq. 1c.

From the point of view of wave propagation, $R\left[\xi, p\right](t, a)$ represents the collection of the seismic traces which would be obtained by sounding the medium with an ensemble of seismic source signals forming a wavelet family. Le Gonidec *et al.* (2002, 2003) have shown that, assuming the validity of the Born approximation, the WR provides the same information on the structure of the medium than the CWT directly applied on the impedance profile $p(z)$. The full equivalence is obtained if the CWT of the impedance profile is computed with the time derivative, ξ', of the analysing wavelet, ξ, used in the WR,

$$a \times R\left[\xi, p\right](t, a) \Leftrightarrow W\left[\xi', p\right](z, a)\,. \tag{2}$$

The $\Leftrightarrow$ symbol is used instead of the $=$ symbol to emphasize the fact that the WR and the CWT of $p(z)$ share the same multiscale properties although they do not belong to the same physical spaces, i.e. time t for the WR and space z for the CWT. This equivalence relationship (2) allows to apply the properties of the CWT to the WR.

The concepts recalled above are illustrated in fig. 1 which considers the case of a reflector formed by a layer of finite thickness, Δz, embedded in a homogeneous half-space. This reflector corresponds to a window impedance profile $p(z)$ (fig. 1a-1) whose CWT (fig. 1a-2) has a global cone-like structure pointing onto the seismic reflector. In the small-dilation domain, this conical pattern splits into two sub-cones, each pointing on an edge of the window. All information necessary to characterize discontinuities is brought by the ridge functions connecting the extrema of the CWT and forming a sparse support in the (z, a) half-plane (Mallat & Hwang, 1992; Alexandrescu *et al.* 1995; Mallat, 1998; Le Gonidec *et al.* 2002). The useful information is obtained through the analysis of the amplitude of the ridges as a function of a as shown in fig. 1a-3. For this particular example, the ridge function of fig. 1a-3 is typical of a step-like discontinuity at small dilations (i.e. slope = 0) and of a Dirac-like singularity at large dilations (i.e. slope = -1). The complicated behaviour of the ridge for intermediate dilations comes from the finite width of the window which controls the dilation a_c where the ridge amplitude has a maximum. More discussion concerning the interpretation of the ridge functions is given by Le Gonidec *et al.* (2002) and Ker *et al.* (2011).

The WR of the same reflector is shown in fig. 1b and, according to eq. (2), it has been multiplied by a and computed with the integral ξ of the wavelet ξ' used to computed the CWT of $p(z)$. By this way, both transforms are equivalent (compare figs. 1a-3 and 1b-3).

In a previous paper, we propose to use the ridge functions as new multiscale seismic attributes to quantify the geometrical characteristics (e.g. thickness) of superficial sediment layers (Ker *et al.*, 2010;

Ker *et al.*, 2011). To achieve this goal, it is of paramount importance that the WR be equivalent to a CWT as stated in eq. (1c). However, such an approach is not possible when dealing with real seismic data, and the limited frequency band of the seismic sources produces distortions of the ridge functions as shown in fig. 1c-3 which represents the WR obtained with a source with a finite bandwidth. These dramatic distortions are due to the fact that the dilated versions of the mother wavelet are no more of the same shape all over the frequency range because of the presence of the seismic source signal $b(t)$ which modifies eq. (1b),

$$R\left[\xi,p\right](t,a) \equiv \mathcal{D}_a\xi(t) * \left[r(t) * b(t)\right] \tag{3a}$$

$$= \left[\mathcal{D}_a\xi(t) * b(t)\right] * r(t) \tag{3b}$$

$$= W\left[\xi,b\right](t,a) * r(t). \tag{3c}$$

These equations show that the experimental WR (eq. 3a), which takes into account the limited source bandwidth, is no more a simple wavelet transform (compare eq. 1b with eq. 3b).

In a first step, Ker *et al.* (2011) dealt with the ridge distortion by performing an empirical correction to validate the relationship between the CWT and the WR methods and estimate reflector thicknesses with the ridge function attributes. This correction consists in normalizing the experimental distorted ridge functions by using the distorted synthetic ridge function of an Heaviside discontinuity.

In the present paper, we propose a more rigorous procedure to correct the experimental ridges like the one in fig. 1c-3 in order to retrieve undistorted ridges as in fig. 1b-3.

3 SOURCE-CORRECTED WAVELET RESPONSE: PRINCIPLES OF THE METHOD

Our approach is similar to the one developed for the wavelet analysis of potential fields to characterize their causative sources by using analysing wavelet belonging to the Poisson semi-group (Moreau *et al.* 1997, 1999; Sailhac *et al.* 2009). The main idea at the root of the method detailed below is to find wavelets ξ such that,

$$\mathcal{D}_a\xi(t) * b(t) = A \times \mathcal{D}_{a_e}\xi_e(t), \tag{4}$$

where ξ_e is an effective analysing wavelet accounting for the effects of the finite frequency band of the seismic source, A is an amplitude function, and a_e is an effective dilation accounting for the time-widening of the initial wavelet ξ produced by the convolution with the filter b (eq. 3b).

3.1 Lévy alpha-stable distribution model for $\xi(t)$ and $b(t)$

We now address the derivation of analysing wavelets $\xi(t)$ satisfying eq. (4), i.e. such that the action of the source filter, $b(t)$, onto the wavelet family $\mathcal{D}_a\xi(t)$ produces the wavelet family $\mathcal{D}_{a_e}\xi_e(t)$ where the dilations a map on a range of effective dilations a_e. We have the following theorem:

Theorem 3.1. Eq. (4) is satisfied if $\xi(t)$ and $b(t)$ are derivatives of order n and m of a Lévy alpha-stable distribution $L(t)$.

Proof. Taking

$$\xi(t) = \frac{\mathrm{d}^n}{\mathrm{d}t^n} L(t), \tag{5}$$

and

$$b(t) = \frac{\mathrm{d}^m}{\mathrm{d}t^m} L(t), \tag{6}$$

where $L(t)$ satisfies the stability property,

$$L\left(\frac{t}{a_1}\right) * L\left(\frac{t}{a_2}\right) = \alpha \times L\left(\frac{t}{a_e}\right), \tag{7}$$

the left-hand term of eq. (4) becomes:

$$\mathcal{D}_a\xi(t) * b(t) = \frac{1}{a} \times \frac{\mathrm{d}^n}{\mathrm{d}(t/a)^n} L\left(\frac{t}{a}\right) * \frac{\mathrm{d}^m}{\mathrm{d}(t/a_b)^m} L\left(\frac{t}{a_b}\right) \tag{8a}$$

$$= \frac{1}{a} \times \frac{a_b^m}{a^m} \times \frac{\mathrm{d}^{n+m}}{\mathrm{d}(t/a)^{n+m}} \left[L\left(\frac{t}{a}\right) * L\left(\frac{t}{a}\frac{a}{a_b}\right) \right] \tag{8b}$$

$$= \frac{\alpha}{a} \times \frac{a^n a_b^m}{a_e^{n+m}} \times \frac{\mathrm{d}^{n+m}}{\mathrm{d}(t/a_e)^{n+m}} L\left(\frac{t}{a_e}\right) \tag{8c}$$

$$= A \times \mathcal{D}_{a_e}\xi_e(t), \tag{8d}$$

where $A = \alpha \times \frac{a_e}{a} \times \frac{a^n a_b^m}{a_e^{n+m}}$ and $\xi_e(t)$ is defined as the $(n+m)\mathrm{th}$ derivative of $L(t)$. The proof terminates by observing that eq. (8d) is equivalent to eq. (4). □

3.2 Gaussian models for $\xi(t)$ and $b(t)$

We now apply the theory explained above with the Lévy alpha-stable Gaussian wavelet family. For this purpose, we derive Gaussian models for both the analysing wavelet, $\xi(t)$, and the source filter, $b(t)$, to satisfy eq. (4). The choice of Gaussian derivative function (GDF) is of a particular interest in the framework of the wavelet transform (Goupillaud *et al.*, 1984; Holschneider, 1995; $n = 2,\, 3\, or\, 4$ are commonly used, see Le Gonidec *et al.*, 2002, 2003 and Ker *et al.*, 2011). Consequently, we take both $\xi(t)$ and $b(t)$ as GDF of order n and m respectively:

$$\mathcal{D}_a\xi(t) = \frac{1}{a}\frac{\mathrm{d}^n}{\mathrm{d}t^n} \exp\left(-\frac{t^2}{a^2}\right), \tag{9}$$

and

$$b(t) = b_0 \frac{d^m}{dt^m} \exp\left(-\frac{t^2}{a_b^2}\right), \tag{10}$$

where b_0 is an amplitude factor and a_b controls the frequency bandwidth of $b(t)$.

Using these expressions, eq. (4) gives,

$$\mathcal{D}_a \xi(t) * b(t) = \frac{2b_0 a_b \sqrt{\pi}}{\sqrt{a^2 + a_b^2}} \frac{\mathrm{d}^l}{\mathrm{d}t^l} \exp\left(-\frac{t^2}{a^2 + a_b^2}\right) \tag{11a}$$

$$= A \times \mathcal{D}_{a_e} \xi_e(t), \tag{11b}$$

where,

$$l = n + m, \tag{12a}$$

$$a_e = \sqrt{a^2 + a_b^2}, \tag{12b}$$

$$A = 2b_0 a_b \sqrt{\pi}, \tag{12c}$$

and the effective analysing wavelet

$$\xi_e(t) = \frac{\mathrm{d}^l}{\mathrm{d}t^l} \exp\left(-t^2\right) \tag{13a}$$

$$= (-1)^l H_l(t) \exp(-t^2). \tag{13b}$$

The Hermite polynomial is defined as (Abramowitz & Stegun, 1972),

$$H_l(t) = (-1)^l \exp\left(t^2\right) \frac{\mathrm{d}^l}{\mathrm{d}t^l} \exp\left(-t^2\right). \tag{14}$$

Expressions for $\xi_e(t)$ up to $l = 10$ are given in appendix A.

Using Gaussian models for both $\xi(t)$ and $b(t)$ allows to further simplify eq. (3b) which rewrites in a form equivalent to eq. (1c),

$$R\left[\xi, p\right](t, a) = A \times \mathcal{D}_{a_e} \xi_e(t) * r(t) \tag{15a}$$

$$= A \times W\left[\xi_e, r\right](t, a_e). \tag{15b}$$

The equations above show that the CWT of a seismic trace with finite frequency bandwidth can be made equivalent to the CWT of the reflectivity function, i.e. the impulse response of the medium $p(z)$, through the rescaling given by eq. (12b). This practically corresponds to the removal of the distortions induced by the source signal $b(t)$ that differs from an impulse signal $\delta(t)$. The rescaling of eq. (12b) accounts for the low-pass nature of the source signal in the sense that the effective CWT, $W\left[\xi_e, r\right]$, spans the reduced range of dilations $a_e \geq a_b$ instead of $\mathbb{R}^+$. Such a result is analogous to what happens for the multiscale analysis of potential fields where the undistorted CWT obtained

with wavelets belonging to the Poisson semi-group is limited to dilations larger than the depth of the causative sources (Moreau *et al.*, 1997 and 1999; Sailhac *et al.*, 2009).

3.3 Example: ridge function topology of a homogeneous layer

We now complete the example of fig. 1 to illustrate the theoretical developments on a homogeneous layer of thickness Δz, i.e. we take into account a limited frequency bandwidth source to perform the WR including the term $b(t)$ (eq. (3a)). For this purpose, we consider a Ricker wavelet, which is a GDF of order 2, for both $\xi(t)$ and $b(t)$ (i.e. $n = m = 2$). The modulus of the WR (fig. 1c2), i.e. the absolute value of eq. (3a), shows distortions procuded by $b(t)$ on the WR defined by eq. (1b) (fig. 1b2). In particular, the ridge function (fig. 1c3) is strongly affected by $b(t)$: at small dilations, the asymptotic behaviour does not correspond to a Heaviside-like discontinuity and the location of the maximum has been shifted.

When we process the WR according to the processing method (eq. (11a), with $l = n+m = 4$), we obtain the WR plotted in fig. 1d2 after amplitude and dilation range corrections. The source-corrected ridge function of fig. 1d3 looks very similar to fig. 1b3 where $b(t)$ is not considered. In particular, the asymptotic behaviour is retrieved with a slope ~ -1 typical of a Dirac discontinuity at large dilations. But the small-dilation domain is reduced by the rescaling given by eq. (12b) and, consequently, the horizontal slope observed in the ridge of fig. 1b3 is not recovered. Other discrepancies are observed in the medium-dilation domain with a more pronounced maximum and the appearance of a tiny minimum which is not present in the ridge of fig. 1b3. These discrepancies must not be attributed to a defect of either the rescaling (eq. 12b) or the amplitude correction (eq. 12c) but, instead, to the fact that the WR is now obtained with the effective wavelet $\xi_e(t)$ (eq. 13a), i.e. a GDF of order $l = 4$ with more oscillations than the analysing wavelet $\xi(t)$.

Depending on the derivative order l of the analysing GDF (figs. 2a-d), the ridge function shows some changes, as illustrated in figs. 2e-h computed for $l = 4, 6, 8, 10$, respectively. Note that the number of extrema in a GDF of order l is $l + 1$. For all ridges, the asymptotic behaviours at small and large scales remain the same, but differences can be observed at intermediate dilations: both the number, the location and the amplitude of the extrema increase with l because of interferences between the wavelet family and the multiscale structure of the discontinuity. In particular, slight shifts of the dilation a_c of the absolute maximum amplitude are due to changes of the shape of $\xi_e(t)$ with l, and the relation between a_c and Δz depends on the wavelet actually used, as detailed in Section 5.3.2 (see eq. 24). As a consequence, the reference WR associated to the source-corrected WR must be a GDF of the same order ($l = 4$), i.e. the efficiency of the source-correction method is highlighted by the perfect agreement between ridge functions of fig. 1d3 and fig. 2e.

4 GAUSSIAN WAVELET MODEL $b(t)$ FOR A HIGH RESOLUTION SEISMIC SOURCE

4.1 Methodology to determine the derivative order m

In the example of section 3.3, the source signal is supposed to be – and indeed is – a perfect GDF, and we now consider the case of real source signals, $s(t)$, whose complicated shape makes impossible to directly find a GDF source model $b(t) \approx s(t)$. The seismic devices used in marine surveys use sources emitting modulated chirps (Quinn *et al.*, 1998) which allow to deconvolve the data so that the resulting post-deconvolution source, $s(t)$, has a flat spectrum in a wide frequency band (see Ker *et al.*, 2010, for explanations on this seismic processing). Now, we instead search for a GDF whose spectrum may be considered contained in the frequency band where the spectrum $\hat{s}(f)$ of $s(t)$ is constant and zero-phase. For such a $b(t)$ we have,

$$b(t) * s(t) \approx b(t), \tag{16}$$

which, in the Fourier domain reads,

$$\hat{b}(f)[1 - \hat{s}(f)] \approx 0. \tag{17}$$

This eq. is satisfied whenever $\hat{b}(f)$ has a compact support contained in the frequency band where $\hat{s}(f) = 1$. For GDF, eq. (16) will be more or less respected depending on the value of a_b and m which control the roll-off of $\hat{b}(f)$ outside the source bandwidth. In a certain sense, $b(t)$ may be considered as a shaping filter which transforms the source $s(t)$ into the desired GDF. In the present case, $s(t)$ can be considered as an identity element for the convolution in a limited frequency bandwidth (i.e zero-phase and flat spectrum), thus both the shaping filter and the GDF are the same $b(t)$.

The determination of b_0, m and a_b (eq. 10) is constrained by the fact that $l = n + m$ must be as low as possible in order to reduce the number of oscillations in the effective wavelet $\xi_e(t)$ (see fig. 2). The retained GDF must also be such that the source model $b(t)$ has a spectrum very near the one of the real seismic source $s(t)$. By this way, we ensure that as much as possible information contained in the original source signal is preserved in the source filter. In practice, we determine a_b and m in the frequency domain by minimizing the quadratic misfit,

$$\mathrm{RMS}(a_b, m) = \int |\hat{b}(f)\,[1 - \hat{s}(f)]\,|^2 \mathrm{d}f. \tag{18}$$

Using the expression of $b(t)$ given by eq. (10), we obtain,

$$\mathrm{RMS}(a_b, m) = \sqrt{\pi} b_0 a_b \int |(2i\pi f)^m \exp[-(\pi a_b f)^2]\,[1 - S(f)]\,|^2 \mathrm{d}f. \tag{19}$$

It is worth to highlight the non-unicity of $b(t)$ as several GDF can respect eq. 16. The choice of the GDF can be fixed by the respect of a threshold of the RMS value and by considering the complexity of the GDF related to its derivative order.

4.2 Particular case of a high resolution seismic source

Even if the processing method described in previous sections can be applied to any kind of source signal, we discuss here the method by considering the example of a high resolution seismic source. Generated by transducers in marine seismics, such a seismic source typically emits a linearly-modulated chirp signal spanning frequencies from f_{low} to f_{high}. According to Ker *et al.* (2010), we suppose a signature deconvolution that compacts the source duration and flattens the frequency spectrum inside the bandwidth $[f_{low}; f_{high}]$. From now, it is obviously necessary to better conform with the terminology used in seismic practice, i.e. a correspondence between dilation and frequency is required.

As described above, we consider a Gaussian derivative function of order m defined by a dilated wavelet of dilation a (dimension of time). Recalling that the Fourier transform of such a Gaussian is a Gaussian, and that the time-derivative translates into a multiplication of the spectrum by $(2i\pi f)^m$ (e.g. Bracewell 1999), the frequency f_{peak} of the GDF is determined from its Fourier transform which has a maximum at (Heigl, 2007):

$$f_{peak} = \frac{1}{\pi a}\sqrt{\frac{m}{2}}, \tag{20}$$

The frequency bandwidth Δf is also a function of both the derivative order m and the dilation a (Ravela & Manmatha; 1999): Δf is larger when m is high and a is low.

In practice, the limits a_{min} and a_{max} are determined in such a way that their corresponding frequencies f_{high} and f_{low}, respectively, given by eq. (20), correctly covers the source spectrum. It is important to observe that the constant frequency range, determined from the source bandwidth, corresponds to a variable dilation range depending on m, as discussed below.

5 SYSIF SOURCE-CORRECTED ANALYSIS OF A HOMOGENEOUS THIN LAYER

The SYSIF seismic device is a deep-towed system developed by Ifremer to image the subseabed with a metric (HR) to sub-metric (VHR) resolution for depth penetrations up to 350 m in a silty clay sediment type. The reader is referred to Ker *et al.* (2010) and Marsset *et al.* (2010) for a detailed presentation of the SYSIF system and the processing of SYSIF seismic data. Actually, two sources are involved in the SYSIF device, so two source filters $b(t)$ have to be defined according to the method proposed in the previous sections, one for the HR and one for the VHR seismic sources. As noted in the previous section, the processing method deals with the deconvolved source signatures: fig. 3 shows these source signals and frequency spectra involved in the present study. We also introduce the effective wavelet $\xi_e(t)$ associated to the seismic SYSIF source and we use it to analyse a synthetic window function discontinuity in order to discuss the method and its limitations when a real seismic source is involved.

5.1 Effective wavelet $\xi_e(t)$ of the SYSIF seismic source

The SYSIF deep-towed seismic device is equipped with two seismic sources covering the high-resolution (HR: $220 < f < 1050$ Hz) and very-high-resolution (VHR: $580 < f < 2200$ Hz) frequency bands. The aim of this section is to determine the parameters a_b and m of the best GDF source wavelet $b(t)$ by computing the RMS of eq. (19) for a range of dilation $a_{min} \leq a_b \leq a_{max}$ and for a range of derivation order $m = 1, \ldots, 10$ of the GDF $b(t)$. Following the method described in section 4, we compute the minimum value of the RMS errors (fig. 4a) and the dilations a_b (figs. 4b,c) for both SYSIF sources. We remember that the dilation range depends on m: for the HR source for instance, $m = 1$ implies $a_{min} = 214$ μs and $a_{max} = 1023$ μs and $m = 10$ gives $a_{min} = 678$ μs and $a_{max} = 3235$ μs. In fig. 4a, we observe that both sources follow similar behaviours, with a strong decrease of the RMS error at $m = 3$. In figs. 4b,c, we observe that a_b increases in the range $[430; 1224\mu s]$ for the HR source and $[250; 549\mu s]$ for the VHR source. To shape the seismic source, $b(t)$ is defined by a derivative order m that is a trade-off between a small value of the RMS error and a low value of a_b: $m = 3$ and $m = 4$ appear as good candidates. The final choice for m may also rely on a visual inspection of the fit in the time domain as in figs. 5a-d where the approximation $b(t) * s(t) \approx b(t)$ appears much better for $m = 4$ than for $m = 3$. In the frequency domain (figs. 5e-h), one can observe the good match between the spectra of $b(t)$ and $b(t) * s(t)$ for both sources excepted at the lower and upper bounds of the bandwidth. This mismatch at the bounds is more pronounced for $m = 3$ than for $m = 4$. The dilation a_b of the source filter of order $m = 4$ is $a_b = 776\mu s$ for HR and $a_b = 357\mu s$ for VHR.

With these parameters, the source filters $b(t)$ take into account the frequency bandwidth limitations of the SYSIF source and can be considered for a multiscale analysis of a discontinuity in the framework of the processed WR (eq. 11b). In order to assimilate the two SYSIF sources as a single seismic source which covers a very large frequency range, we merge both the HR and VHR WRs. To do so, a common order m is mandatory for both $b(t)$ models of the SYSIF device.

The WR analysis deals with both the source filter $b(t)$ and the analysing wavelet $\xi(t)$, through the effective wavelet $\xi_e(t)$ which complexity is related to its derivative order l. The analysing wavelet $\xi(t)$ is taken as GDF of order $n = 1$ to minimize the order l. As a conclusion, the effective wavelet $\xi_e(t)$ of the merged SYSIF sources is a GDF of order $l = 5$.

5.2 Discussions on the effective dilation range of the merged SYSIF source

At this stage of the discussion, it is worth recalling that dimensionless relative dilations a_r are often more comfortable to use for practical computations instead of absolute dilations a. In the previous paper Ker *et al.* (2011), we defined $a_r = \lambda/\lambda_0$ with λ and λ_0 the wavelengths of the dilated and

mother wavelets, respectively, i.e. $a_r = a/a_0$ where a_0 is a reference time unit related to a frequency sampling rate. In the following, we present the results in terms of dimensionless relative dilations, with the sampling rate involved in the SYSIF device ($1/a_0 = 10kHz$).

In the remaining of this paper, the effective wavelet $\xi_e(t)$ is a GDF of order $l = 5$ with a frequency $f_{peak} = 5033$ Hz given by eq. 20 with $a = a_0$ and $m = l$. In this section, the wavelength is $\lambda_{peak} = 29.8$ cm (for a *P*-wave velocity $V_p = 1500$ m/s). The effective dilation a_e depends on the dilation a_b of the source filter, different for the HR and for the VHR $b(t)$ models (eq. 10). This leads to two different dilation ranges, noted $\mathcal{R}_{a_r}^{\mathrm{HR}}$ and $\mathcal{R}_{a_r}^{\mathrm{VHR}}$, where a_r refers now to the dimensionless dilation a_e/a_0 according to Ker *et al.* (2011). Similarly, we note $\mathcal{R}_f^{\mathrm{HR}}$ and $\mathcal{R}_f^{\mathrm{VHR}}$ the associated frequency ranges, which represent the physical peak frequency of the effective wavelet $\xi_e(t)$. When both SYSIF sources are merged into one broadband source, we note:

$$\mathcal{R}_{a_r} = \mathcal{R}_{a_r}^{\mathrm{HR}} \cup \mathcal{R}_{a_r}^{\mathrm{VHR}}, \tag{21a}$$

$$\mathcal{R}_f = \mathcal{R}_f^{\mathrm{HR}} \cup \mathcal{R}_f^{\mathrm{VHR}} \tag{21b}$$

for the global effective dilation range (eq. 21a) and accordingly, the associated frequency ranges (eq. 21b).

It is important to remember that the lower bounds of $\mathcal{R}_{a_r}^{\mathrm{HR}}$ and $\mathcal{R}_{a_r}^{\mathrm{VHR}}$ are fixed by the dilations a_b of the source filters $b(t)$. On the other hand, the upper bounds are not constraint but the lack of low frequency content of $b(t) * s(t)$ for both SYSIF sources (see Figs. (5g,h)) introduces distortions in the dilated wavelets. These distortions, more and more pronounced when dilations increase, can be quantified with a relative rms error related to the consideration of $\xi_e(t)$, a GDF of order $l = 5$ and an effective dilation $a_e \geq a_b$, instead of an analysing wavelet $\xi(t)$ of the same order $n = l$ but with dilations $a \in \mathbb{R}^+$. We define the maximum value of this relative rms error such that $\mathcal{R}_{a_r}$ is continuous, i.e. the upper bound of $\mathcal{R}_{a_r}^{\mathrm{HR}}$ joins the lower band of $\mathcal{R}_{a_r}^{\mathrm{VHR}}$: this condition $\mathcal{R}_{a_r,max}^{\mathrm{HR}} \sim \mathcal{R}_{a_r,min}^{\mathrm{VHR}}$ is satisfied with a threshold of 20% on the relative error.

The relation between the absolute dilation a, detailed in the formalism of section 3 and expressed in μs, versus the dimensionless dilation $a_r = a_e/a_0$, is shown in figs. 6a,b. With a rms threshold of 20%, $\mathcal{R}_{a_r}^{\mathrm{HR}} = [7.84; 17.64]$ and $\mathcal{R}_{a_r}^{\mathrm{VHR}} = [3.74; 7.61]$. According to eq. 20, the associated frequency ranges are shown in figs. 6c,d: $\mathcal{R}_f^{\mathrm{HR}} = [285; 642$ Hz$]$ and $\mathcal{R}_f^{\mathrm{VHR}} = [600; 1345$ Hz$]$. It is interesting to note that the effective frequency ranges overlap, even if the dilation ranges do not. As a conclusion, we get:

$$\mathcal{R}_{a_r} = [3.74; 17.64], \tag{22a}$$

$$\mathcal{R}_f = [285; 1345Hz]. \tag{22b}$$

5.3 Source-corrected seismic attributes of a thin homogeneous layer

5.3.1 Processed WR and ridge function of the thin layer

In this section, we compute the synthetic seismic dataset of a window function discontinuity analysed simultaneously with the HR and the VHR sources of the SYSIF device. The synthetic seismic dataset is computed for a homogeneous layer thickness $\Delta z = 45cm$, which associated Green's function is computed from a method based on the Goupillaud's model (1961) (see Ker *et al.* 2011 for details on the forward modelling). The reference continuous WR of the discontinuity, defined for $a \in \mathbb{R}^+$, is performed with an analysing wavelet $\xi(t)$ with a derivative order $n = 5$ (fig. 7a). When the SYSIF source is taken into account, the corresponding WR$_e$ is computed with an effective wavelet $\xi_e(t)$ of order $l = 5$ which dimensionless effective dilation is $a_r \in \mathcal{R}_{a_r}$, shown in fig. 7b. Since ξ and ξ_e are both based on a GDF of the fifth order ($f_{peak} = 5033$ Hz), WR and WR$_e$ can be directly compared in the common dilation range $\mathcal{R}_{a_r}$.

As discussed in the previous section, the transition between the HR and the VHR components shows some imperfections (fig. 7b), i.e. the amplitude continuity and the distortions of the analysing wavelets in the intermediate band correspond to larger errors of the correction processing. Nevertheless, we observe a very good agreement between both time-scale maps, WR and WR$_e$. The shapes of the raw HR and VHR ridge functions of WR$_e$, i.e. ridge functions not corrected from the distortions induced by the source, are shown in fig. 8a. When we apply the amplitude factor correction (eq. 12c) and display the results versus the effective dilation a_e (eq. 12b), the processed ridge functions are in perfect agreement with the reference, even for rms errors up to 20% (fig. 8b): the solid line corresponds to the reference WR and the symbols to the WR$_e$ (HR in red, VHR in blue). This illustrates the efficiency of the method developed here to remove the WR distortions induced by limited frequency bandwidth sources.

We remember that in section 5.1, the derivative order m of the Gaussian filter $b(t)$ of the source has been justified by a better match with a GDF for $m = 4$ than for $m = 3$. Compare to the case $m = 4$ shown in fig. 8b, the processing quality for $m = 3$ fails to reproduce exactly the shape of the reference ridge function, computed for $n = 4$, as shown in fig. (9). This mismatch confirms that the fourth derivative order is the smallest order that can be used to obtain an appropriate Gaussian filter adapted to SYSIF sources. The methodology to select the derivative order m is efficient and enables to remove the WR distortions induced by SYSIF seismic sources: this analysis of a window function may be included in the processing workflow used to define this filter as a final quality control.

5.3.2 Thin layer thickness based on the seismic attributes

In Ker *et al.* (2011), we have suggested that a multiscale attribute based on the ridge function can inform about the structure of a discontinuity which characteristic size Δz is identified from the dimensionless dilation a_c associated to the maximum amplitude of the ridge function, easier to point when dealing with real seismic data. According to this previous work, we can write:

$$\Delta z = \lambda_c / \beta \tag{23}$$

where β is a dimensionless proportionality factor specific to the considered wavelet, and the wavelength $\lambda_c = V_p / f_{peak,c} = V_p \pi a_c a_0 \sqrt{\frac{2}{l}}$ (eq. 20 with $a = a_c \times a_0$). We can then relate the characteristic size of the reflector to the dimensionless dilation a_c:

$$\Delta z = \frac{a_c}{\beta} \lambda_{peak}, \tag{24}$$

For $\Delta z = 45cm$, we identify $ln(a_c) = 1.93$ from the ridge function shown in fig. 8b, i.e. we are able to define $\beta = 4.57$ for a GDF of order $l = 5$. Note that in Ker *et al.* (2011), we worked with $\beta = 2.61$ in the CWT with Ricker wavelets ($l = 2$), in agreement with the literature on such seismic wavelets (Kallweit & Wood, 1982 and Chung & Lawton, 1995): for a GDF wavelet $l = 5$, no literature exists on the subject but the approach is the same to define the associated β value. In the remaining of this section, we use the relation $\Delta z = a_c / 15.33$ to define the characteristic size of a complex discontinuity in the framework of the wavelet transform (see Appendix B for an extension to the dominant wavelength representation).

In the present work, we show that the merged WR_e of the SYSIF sources is defined in the effective dilation range $\mathcal{R}_{a_r}$, i.e. $a_c \in [3.74; 17.64]$. Accordingly, the SYSIF device can be used to identify seismic reflector thicknesses $\Delta z \in \mathcal{R}_{\Delta_z}$, where the range is defined by

$$\mathcal{R}_{\Delta_z} = [24; 115cm]. \tag{25}$$

Thicknesses smaller than 24 cm, as illustrated in Fig. 10a for $\Delta z = 22$ cm, can not be estimated from a_c as the effective dilation is restricted to the decreasing part of the ridge function with a slope close to -1. In that case, a thin layer can be approximated to a Dirac discontinuity with no characteristic size. Nevertheless, the segment of ridge function limited to $\mathcal{R}_{a_r}$ is not a perfect straight line, suggesting the presence of a complex structure rather than a pure Dirac discontinuity.

In the range $\mathcal{R}_{\Delta_z}$, the layer thickness is determined from the dilation a_c of the maximum of the ridge function following eq. (24). Within this range, the location of a_c can be correctly identified (see fig. 8b for $\Delta z = 45$ cm and the associated WR_e in fig. 7b). Consequently, good estimation of a_c can be attempted when accepting correction rms errors up to 20%. Close to the upper bound, the case $\Delta z = 112$ cm is shown in fig. 10b where a very good agreement between the reference and the

source-corrected ridge functions is still observed, even in the complex part of the ridge function where interference phenomena occur. From such seismic attributes, the layer thickness Δz is perfectly given by the dilation located at $ln(a_c) = 2.84$, according to eq. 24. Note that it is theoretically possible to relate Δz to other extrema of the ridge function, such as the minimum amplitude (Le Gonidec *et al.*, 2003), but a maximum is easier to identify in real seismic data.

For thicknesses larger than 115 cm, the dilation a_c can not be identified since it is out of the effective dilation range which is on the left hand side of the maximum amplitude, i.e. where the internal structure is detected. This dilation range covers the Heaviside asymptotic behaviour and the multiscale attributes analysis may become useless as a direct estimation of the thickness can be made by a straightforward interpretation of the seismograms.

6 APPLICATION TO COMPLEX SUB-SURFACE SEDIMENTARY LAYERS

We now assess the multiscale seismic attributes to analyse superficial deep-sea hemipelagic sediments from the seismic datasets detailed in Ker *et al.* (2011): one concerns synthetic seismic traces, computed with a forward modelling on *in situ* and core measurements, and the other concerns seismic traces acquired at sea by the SYSIF deep-towed device in the close vicinity of the ground truth data. In Ker *et al.* (2011), this case study shows a very good match between the subsurface structure described from the ground truth data and the seismic reflectors.

6.1 Source-corrected seismic attributes of the impedance log defined from ground truth data

In this section, we work on a synthetic WR of the subseabed: from ground truth data, we define the *in situ* acoustic impedance log of the subsurface used to compute the Green's function of the structure (fig. 11a). The analysis is based on two steps, presented in section 5.3 for a window discontinuity. First, we use eq. 1a to compute the reference continuous WR of the subsurface with an unlimited frequency bandwidth seismic source, i.e. for dilations $a \in \mathbb{R}^+$. This WR, displayed in fig. 11b, shows numerous cone-like structures pointing toward the position of seismic reflectors. Second, we use eq. 3a to numerically sound the subsurface with the SYSIF device, taken into account with $b(t)$, which limited frequency bandwidth induces distortions in the seismic attributes: we apply the source-correction method to remove these distortions and perform the effective wavelet response WR_e (fig. 11c). Note that WR_e is defined in the limited and dimensionless dilation range $\mathcal{R}_{a_r}$, which corresponds to the frequency range $[285; 1345Hz]$ (see eqs. 22a and 22b).

In the common dilation range, we observe a very good agreement between the reference WR and the source-corrected WR_e maps (figs. 11b and 11c, respectively). In particular, the two reflectors A and

B already introduced in Ker *et al.* (2011) can be identified (dashed lines) from cone-like structures that point towards them. Since the WR and the WR_e are associated to the same GDF ($l = 5$), the associated ridge functions can be plotted versus the same dimensionless dilation, the reference curve in solid line and the source-corrected curve in symbols (figs. 11(d,e)). The very good agreement between the curves puts in evidence the efficiency of the source-correction method which allows to analyse a complex structure with quantitative descriptions based on the multiscale seismic attributes. For instance, the maximum of the ridge function indicates the characteristic size of the seismic reflectors A and B: according to eq. 24, $\Delta z^A = 85$ cm and $\Delta z^B = 99$ cm, respectively (uncertainties estimated to ± 2 cm and $V_p = 1485 m/s$).

6.2 Source-corrected seismic attributes of superficial sediment structures: SYSIF seismic data

In this section, we work on field seismic traces, i.e. the data acquired at sea with the SYSIF seismic device and we perform the source-correction processing to compute the effective wavelet response WR_e of superficial structures (fig. 12a). As in the previous synthetic analysis, reflectors A and B can be identified, plotted in dashed lines in the WR_e map. Note that in this case, no continuous reference wavelet response can be associated to the results. Nevertheless, since the seismic traces have been acquired at the same site than the ground truth data used in the previous analysis, the results can be compared to the synthetic results displayed in fig. 11b. We observe a good agreement between both approaches. In particular, the ridge functions associated to reflectors A and B (figs. 11b,c) are in good agreement with the synthetic results and the characteristic sizes are $\Delta z^A = 89$ cm and $\Delta z^B = 100$ cm, respectively.

6.3 Discussions

Results obtained in section 6.1 validate the source-correction processing and even in the case of complex seismic signals, we are able to remove the distortions induced by real seismic sources. We highlight that the analysis based on both seismic and ground truth data are in very good agreement, which indicates the robustness of the method. In particular, the characteristic sizes of reflectors A and B estimated from these two approaches are in good accordance. In the previous work (Ker *et al.*, 2011), the empirical correction gives a satisfactory thickness estimation for both reflectors, $\Delta z^A = 81$ cm and $\Delta z^B = 99$ cm (to compare with the present source-corrected results $\Delta z^A = 89$ cm and $\Delta z^B = 100$ cm) but the distortion residuals of the ridge function remain strong and do not allow to use the whole ridge function as a correct multiscale seismic attributes.

The source-corrected method applied on seismic SYSIF data confirms the efficiency of the multiscale analysis, despite the structure complexity of the subsurface and the limited frequency bandwidth

of the seismic sources. It is important to highlight that this powerful data processing allows to work not only with the characteristic size of a seismic reflector but also with the global shape of the processed ridge function, i.e. with the full content of the multiscale attributes.

7 CONCLUDING REMARKS

Real seismic sources are characterized by limited frequency bandwidths, i.e. they act as band-pass filters $b(t)$ which distort the multiscale seismic attributes based on the wavelet response (WR), as introduced in Ker *et al.* (2011). In the present paper, we present a source-corrected method used to remove such distortions induced by a seismic source. In a way similar to the wavelet analysis of potential field performed with the Poisson wavelet semi-group (Moreau *et al.*, 1997 and 1999; Sailhac *et al.*, 2009), we work with Lévy alpha-stable distributions in order to define an effective analysing wavelet $\xi_e(t)$ accounting for the source effects. The wavelets considered here are Gaussian derivative functions (GDF), both for the analysing wavelet family $\mathcal{D}_a\xi(t)$ (order n and dilation a) and for the source filter $b(t)$ (order m and dilation a_b), i.e. the convolution $\mathcal{D}_a\xi(t) * b(t)$ results in an effective wavelet family $\mathcal{D}_{a_e}\xi_e(t)$ which is a GDF of order $l = n+m$ with an effective dilation $a_e = \sqrt{a^2 + a_b^2}$. Note that a_e does not span in $\mathbb{R}^+$ but $a_e > a_b$. The multiscale analysis based on this effective GDF - scaled with an amplitude factor depending on a_b and displayed versus a_e accounting for the time-widening of $\xi(t)$ when convolved with the source filter $b(t)$ - allows to work with source-corrected ridge functions.

In order to define the Gaussian filter that reshapes the seismic source, i.e. the GDF required to perform the undistorted WR, two parameters have to be determined: the derivative order m and the dilation a_b. For both SYSIF deep-towed seismic sources (HR and VHR), we find that the associated GDF are both defined with $m = 4$ and different a_b. We consider $n = 1$ for $\xi(t)$ to minimize the complexity of the effective analysing wavelet, which order is then $l = 5$ and a_e spans in a reduced dilatation range. To cover all dilations between the HR and VHR sources, which frequency bandwidths overlap, we define a maximum rms error value of 20% between the effective wavelet associated to the SYSIF sources (GDF of order $l = 5$ and $a_e > a_b$) and the associated equivalent $\xi(t)$ (GDF of order $l = 5$ and $a \in \mathbb{R}^+$), i.e. we accept some disagreements of the dilated wavelets. Applied on a window function, the SYSIF WR is in very good accordance with a reference WR computed without the source limitation. This agreement is highlighted by the comparison of the ridge functions which are similar in the dilation range covered by the SYSIF sources and associated to layer thicknesses in the range [24;115 cm].

We work on both synthetic and field seismic traces. We define the former from ground truth data related to deep-water hemipelagic sediments and we take into account the SYSIF source properties to

perform the source-corrected WR. We compare the results with a reference WR, i.e. without any source limitation, and we show very good accordances. In particular, the seismic attributes of reflectors A and B indicate layer thicknesses of 85 and 99 cm, respectively: the multiscale analysis of the acoustic impedance log is in perfect agreement with the synthetic WR corrected from distortions induced by the SYSIF sources. In the close vicinity of the ground truth data, SYSIF field seismic data are also available to perform the undistorted WR analysis: the ridge functions associated to reflectors A and B are very similar to the ones performed with the synthetic traces, providing the same layer thicknesses.

The theoretical context of the source-corrected wavelet response, enhanced by the first application on seismic data, evidences a major improvement to quantify multiscale seismic attributes, despite the complexity of the reflectors and the limited frequency bandwidth of the source. This multiscale processing allows to work with the global shape of the source-corrected ridge function and is promising to go further into such seismic attributes analysis.

Actually, we highlight that the WR source-corrected processing can be applied not only with the SYSIF device but with any kind of source signal device which signature is well known and stable. This method, based on the theoretical framework of the wavelet transform, has potentiel interests for many physical applications, such as Non Destructive Testing (NDT) performed with ultrasonics or electromagnetic measurements. In particular, the method can be used to perform a source-corrected experimental WR by the use of a single broad-band source signal, i.e. an extension of the wavelet response introduced by Le Gonidec *et al.* (2002).

APPENDIX A

The effective wavelet can be expressed as eq. 13a and 13b:

$$\xi_e(t) = \frac{\mathrm{d}^l}{\mathrm{d}t^l} \exp\left(-t^2\right) \tag{26a}$$

$$= (-1)^l H_l(t) \exp(-t^2). \tag{26b}$$

The Hermite polynomial is defined as (Abramowitz & Stegun, 1972),

$$H_l(t) = (-1)^l \exp\left(t^2\right) \frac{\mathrm{d}^l}{\mathrm{d}t^l} \exp\left(-t^2\right). \tag{27}$$

The expressions of the first tenth Hermite polynomials are now given in eqs. 28 to 37.

$$H_1(t) = (2t) \tag{28}$$

$$H_2(t) = \left(4t^2 - 2\right) \tag{29}$$

$$H_3(t) = \left(8t^3 - 12t\right) \tag{30}$$

$$H_4(t) = \left(16t^4 - 48t^2 + 12\right) \tag{31}$$

$$H_5(t) = \left(32t^5 - 160t^3 + 120t\right) \tag{32}$$

$$H_6(t) = \left(64t^6 - 480t^4 + 720t^2 - 120\right) \tag{33}$$

$$H_7(t) = \left(128t^7 - 1344t^5 + 3360t^3 - 1680t\right) \tag{34}$$

$$H_8(t) = \left(256t^8 - 3584t^6 + 13440t^4 - 13440t^2 + 1680\right) \tag{35}$$

$$H_9(t) = \left(512t^9 - 9216t^7 + 48384t^5 - 80640t^3 + 30240t\right) \tag{36}$$

$$H_{10}(t) = \left(1024t^{10} - 23040t^8 + 161280t^6 - 403200t^4 + 302400t^2 - 30240\right) \tag{37}$$

A mathematical framework on Hermite polynomials can be found in Kreyszig (1978).

Appendix B

In the framework of the wavelet transform, ridge functions correspond to the extrema of the CWT as a function of the dilation a of the dilated wavelet. This is the representation chosen in the present work but it is interesting to plot the results with respect to the peak wavelength λ_{peak}, inversely proportional to f_{peak} (see eq. 20), and to the dominant wavelength λ_d, commonly used in seismology. For λ_{peak}, the peak frequency f_{peak} is uniquely defined in the wavelet spectrum as the frequency of the largest amplitude. The dominant wavelength λ_d is related to the breadth of the wavelet (Kallweit & Wood, 1982) which is defined as the time between two secondary extrema close to the central lobe of a symmetrical wavelet (even derivative order l, i.e. for a Ricker wavelet $l = 2$, the breadth is defined

by a trough-to-trough time). For asymmetrical wavelets (odd l values), we define the breadth of the wavelet as twice the time between the two primary extrema.

To illustrate the three representations, we plot the ridge function of a thin homogeneous layer (see Fig. 1) analyzed with GDF wavelets of orders $l = 2, 3, 4, 5$, respectively. For the natural representation of the ridge function plotted versus a (figs. B1(a-d)), the location of the maximum shifts with respect to the derivative order l, in accordance with fig. 2. This shift also exists when the ridge function is plotted versus λ_{peak} (figs. B1(e-h)). In the last representation, we observe that the maximum of the ridge function plotted versus the dominant wavelength λ_d remains at a position independent of the derivative order l (figs. B1(i-l)) and corresponds to $\lambda_{d,max} = 4\Delta z$.

ACKNOWLEDGMENTS

We would like to thank the reviewers for their constructive suggestions. This is IPGP contribution number ****.

REFERENCES

Abramowitz, M., & Stegun, I.A., 1972. Handbook of mathematical functions: U.S. Department of Commerce.

Alexandrescu, M., Gibert, D., Hulot, G., Le Mouël, J.-L. & Saracco, G., 1995. Detection of geomagnetic jerks using wavelet analysis, *J. Geophys. Res.*, **100**, 12557-12572.

Banik, N. C., Lerche, I. & Shuey, R. T., 1985. Stratigraphic filtering, Part 1: Derivation of the O'Doherty-Anstey formula, *Geophysics*, **50**, 2768-2774.

Barnes, A.E., 2001. Seismic attributes in your facies, *CSEG Recorder*, **26**, 41-47.

Bracewell, R.N., 1999. *The Fourier transform and its applications*, McGraw-Hill Science/Engineering/Math, New York, 3d ed., 640 pp.

Burridge, B. Papanicolaou, G. & White , B, 1988. One-dimensional wave propagation in a highly discontinuous medium, *Wave Motion*, **10**, 19-44.

Castagna, J., Sun, S. & Siegfried, R.W., 2003. Instantaneous spectral analysis: Detection of low-frequency shadows associated with hydrocarbons, *The Leading Edge*, **22**, 120-127.

Chopra, S., Castagna, J. & Portniaguine, O., 2006. Seismic resolution and thin-bed reflectivity inversion, *CSEG Recorder*, **31**, 19-25.

Chung, H-M. & Lawton, D.C., 1995. Amplitude responses of the thin beds: Sinusoidal approximation versus Ricker approximation, *Geophysics*, **60**, 223-230.

Fomel, S., 2007. Local seismic attributes, *Geophysics*, **72**, A29-A33, doi: 10.1190/1.2437573.

Gastaldi, C., Biguenet, J.-P. & De Pazzis, L., 1997. Reservoir characterization from seismic attributes: An example from the Peciko Field (Indonesia), *The Leading Edge*, **16**, 263-266.

Gesret, A., Laigle, M., Diaz, J., Sachpazi M. & Hirn, A., 2010. The oceanic nature of the African slab subducted

under Peloponnesus: thin-layer resolution from multiscale analysis of teleseismic P-to-S converted waves, *Geophys. J. Int.*, **183**, 833-849.

Goupillaud, P., 1961. An approach to inverse filtering of near-surface layer effects from seismic records, *Geophysics*, **26**, 754-760.

Goupillaud, P., Grossmann, A. & Morlet, J., 1984. Cycle-octave and related transforms in seismic signal analysis, *Geoexploration*, **23**, 85-102.

Heigl, W. M., 2007. Computing Gaussian derivative waveforms of any order, *Geophysics*, **72**, doi:10.1190/1.2716624.

Holschneider, M., 1995. Wavelets: An analysis Tool, 423 pp, Clarendon, Oxford, England.

Kallweit, R.S. & Wood, L.C., 1982. The limits of resolution of zero-phase wavelets, *Geophysics,*, **47**, 1035-1046.

Ker, S., Marsset, B., Garziglia, S., Le Gonidec, Y., Gibert, D., Voisset & M., Adamy, J., 2010. High-resolution seismic imaging in deep sea from a joint deep-towed/OBH reflection experiment: application to a Mass Transport Complex offshore Nigeria, *Geophys. J. Int.*, **182**, 1524-1542.

Ker, S., Le Gonidec, Y., Gibert, D., and Marsset, B., 2011. Multiscale seismic attributes: a wavelet-based method and its application to high-resolution seismic and ground truth data, *Geophys. J. Int.*, **187**, 1038-1054.

Kreyszig, E., 1978. Introductory functional analysis with applications: John Wiley & Sons, Inc.

Le Gonidec, Y., Gibert, D. & Proust, J-N, 2002. Multiscale analysis of waves reflected by complex interfaces: Basic principles and experiments, *J. Geophysic. Res.,*, **107**(B9), 2184, doi:10.1029/2001JB000558.

Le Gonidec, Y., Conil, F. & Gibert, D., 2003. The wavelet response as a multiscale NDT method, *Ultrasonics*, **41**, 487-497.

Mallat, S. & Hwang W. L., 1992. Singularity detection and processing with wavelets, *IEEE Trans. Inf. Theory*, **38**, 617-643.

Mallat, S., 1998, A wavelet tour of signal processing, 2nd ed.: Academic Press Inc.

Marsset, T., Marsset, B., Ker, S., Thomas, Y. & Le Gall, Y., 2010. High and very high resolution deep-towed seismic system: Performance and examples from deepwater Geohazard studies. Deep-Sea Research I, doi:10.1016/j.dsr.2010.01.001.

Moreau F., Gibert, D., Holschneider, M. & Saracco, G., 1999. Identification of sources of potential fields with the continuous wavelet transform: Basic theory, *J. Geophys. Res.*, **104**, 50035013.

Moreau, F., Gibert, D., Holschneider, M. & Saracco, G., 1997. Wavelet analysis of potential fields, *Inv. Problems*, **13**, 165-178.

Morlet *et al.*, 1982. Wave propagation and sampling theory – Part I: Complex signal and scattering in multilayered media, *Geophysics*, **47**, 203, doi:10.1190/1.1441328.

Pennington, W. D., 2001. Reservoir geophysics, *Geophysics*, **66**, 25-30.

Quinn, R., Bull, J.M. and Dix, J.K., 1998. Optimal Processing of Marine High-Resolution Seismic Reflection (Chirp) Data. *Marine Geophysical Researches*, **20**, 13-20.

Ravela, S. and Manmatha, R. 1999. Gaussian Filtered Representations of Images. Wiley Encyclopedia of Elec-

trical and Electronics Engineering.

Sailhac, P., Gibert, D. & Boukerbout, H., 2009. The theory of the continuous wavelet transform in the interpretation of potential fields: A review, *Geophys. Prosp.*, **57**, 517-525, doi: 10.1111/j.13652478.2009.00794.x.

Sheriff, R. E., 1992. Reservoir geophysics: Society of Exploration Geophysicists, Tulsa.

Sultan, N., Voisset, M., Marsset, T., Vernant, A. M., Cauquil, E., Colliat, J. L. & Curinier, V., 2007a. Detection of free gas and gas hydrate based on 3D seismic data and cone penetration testing: An example from the Nigerian Continental Slope, *Marine Geology*, **240** (1-4), 235-255.

Voit, J., 2003. The Statistical Mechanics of Financial Markets (Texts and Monographs in Physics). Springer-Verlag. ISBN 3-540-00978-7.

Widess, M. A., 1973. How thin is a thin bed?, *Geophysics*, **38**, 1176-1180.

Wood, W., Gettrust J.F. & Spychalski, S., 2003, A new deep-towed, multi-channel seismic system. *Sea Technology*, **44**, 44-49.

FIGURE CAPTIONS

Figure 1: Multiscale analysis of a window discontinuity of thickness $\Delta z = 60cm$. (a, left to right): Complex discontinuity, modulus of the continuous wavelet transform (CWT) in the depth-dilation domain with a GDF of order $n = 3$, and ridge function. (b, left to right): Complex discontinuity, modulus of the wavelet response (WR) in the time-dilation domain with a GDF of order $n = 2$, and ridge function. (c, left to right): Complex discontinuity, modulus of the WR when a limited frequency bandwidth source is taken into account ($n = 2$, $m = 2$, $a_b = 318\mu s$ and $b_0 = 1$), and raw ridge function. (d, left to right): Complex discontinuity, modulus of the source-corrected WR ($l = 4$) versus the effective dilation a_e, and source-corrected ridge function.

Figure 2: (a-d) Analysing wavelets with derivative orders $n = 4, 6, 8, 10$, respectively. (e-h) Associated ridge functions computed for a window function.

Figure 3: SYSIF seismic sources: The HR (a) and the VHR (b) deconvolved signatures cover the $220 - 1050Hz$ (b) and $580 - 2200Hz$ (d) frequency bands, respectively.

Figure 4: a) Minimum RMS errors versus the derivative order m, for both the SYSIF HR source (stars) and the SYSIF VHR source (circles) and (b,c) the corresponding dilation a_b.

Figure 5: Comparison between $b(t) * s(t)$ (blue) and $b(t)$ (red). In the time domain: (a) HR, $m = 3$; (b) VHR, $m = 3$; (c) HR, $m = 4$; (d) VHR, $m = 4$. In the frequency domain: (e) HR, $m = 3$; (f) VHR, $m = 3$; (g) HR, $m = 4$; (h) VHR, $m = 4$.

Figure 6: Absolute dilation and peak frequency ranges of the SYSIF HR (on the left) and VHR (on the right) sources, plotted versus the dimensionless dilation $a_r = a/a_0$ for a rms threshold of 20%.

Figure 7: WR of a window function $\Delta z = 45$ cm analysed (a) with the reference wavelet ($n = 5$, $a \in \mathbb{R}^+$), and (b) with the effective wavelet ($l = 5$, $a_r \in \mathcal{R}_{a_r} = \mathcal{R}_{a_r}^{\mathrm{HR}} \cup \mathcal{R}_{a_r}^{\mathrm{VHR}}$) wich takes into account the limited frequency bandwidth of the HR and VHR SYSIF sources.

Figure 8: Ridge functions extracted from the SYSIF WR_e ($l = 5$) for a window function $\Delta z = 45\ cm$ (HR in red, VHR in blue, reference ($n = 5$) in solid line): (a) raw version in the reference dilation range and (b) source-corrected version in the effective dilation range ($m = 4$).

Figure 9: Ridge function extracted from the effective WR_e ($l = 4$) for a window function $\Delta z = 45\ cm$ computed with a source filtering $b(t)$ of the third order ($m = 3$) (HR in red, VHR in blue, reference ($n = 4$) in solid line).

Figure 10: Ridge functions extracted from the SYSIF WR_e ($l = 5$) for window functions of thicknesses (a) $\Delta z = 22\ cm$ and (b) $\Delta z = 112\ cm$ (HR in red, VHR in blue, reference ($n = 5$) in solid line).

Figure 11: Seismic attributes from the Green's function of hemipelagic sediment impedance (synthetic seismic data): (a) impedance profile, (b) reference WR ($n = 5$, $a \in \mathbb{R}^+$), (c) effective SYSIF

WR$_e$ ($l = 5$, $a_r \in \mathcal{R}_{a_r}$) and (d,e) ridge functions of reflectors A and B (WR in solid line and source-corrected WR$_e$ in symbols: HR in red and VHR in blue).

Figure 12: Seismic attributes from field SYSIF data: (a) effective SYSIF WR$_e$ ($l = 5$, $a_r \in \mathcal{R}_{a_r}$) and (b,c) source-corrected ridge functions of reflectors A and B (HR in red and VHR in blue).

Figure 13: Ridge functions of a window discontinuity analyzed with wavelets of derivative orders $l = 2, 3, 4, 5$ (from top to bottom). The curves are plotted versus the dilation (left), the peak wavelength (middle) and the dominant wavelength (right). Black crosses indicate the location of the maximum: note that for the left and middle columns, this location depends on l whereas it is fixed when the ridge function is plotted versus the dominant wavelength.

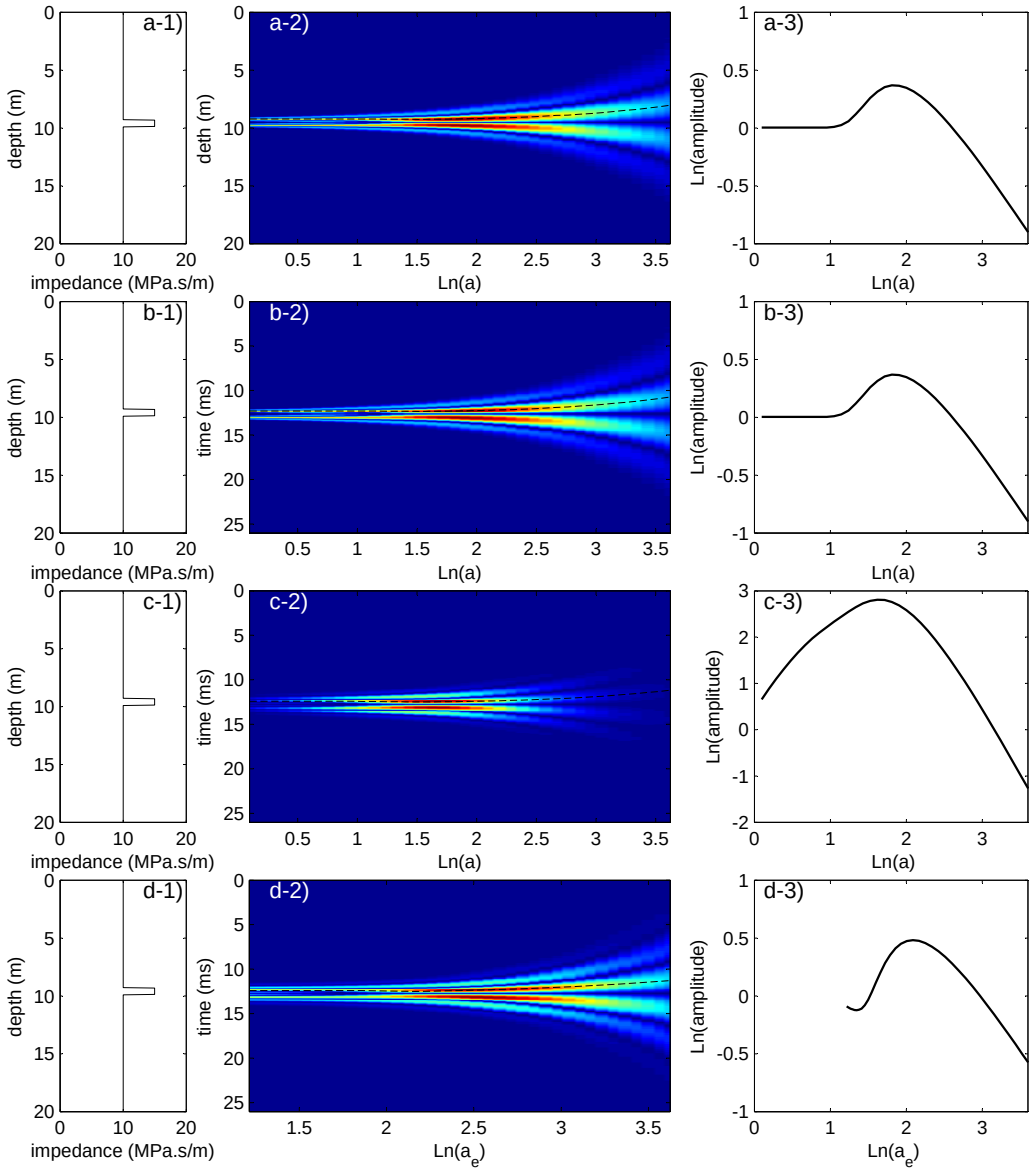

Figure 1. Multiscale analysis of a window discontinuity of thickness $\Delta z = 60cm$. (a, left to right): Complex discontinuity, modulus of the continuous wavelet transform (CWT) in the depth-dilation domain with a GDF of order $n = 3$, and ridge function. (b, left to right): Complex discontinuity, modulus of the wavelet response (WR) in the time-dilation domain with a GDF of order $n = 2$, and ridge function. (c, left to right): Complex discontinuity, modulus of the WR when a limited frequency bandwidth source is taken into account ($n = 2$, $m = 2$, $a_b = 318\mu s$ and $b_0 = 1$), and raw ridge function. (d, left to right): Complex discontinuity, modulus of the source-corrected WR ($l = 4$) versus the effective dilation a_e, and source-corrected ridge function.

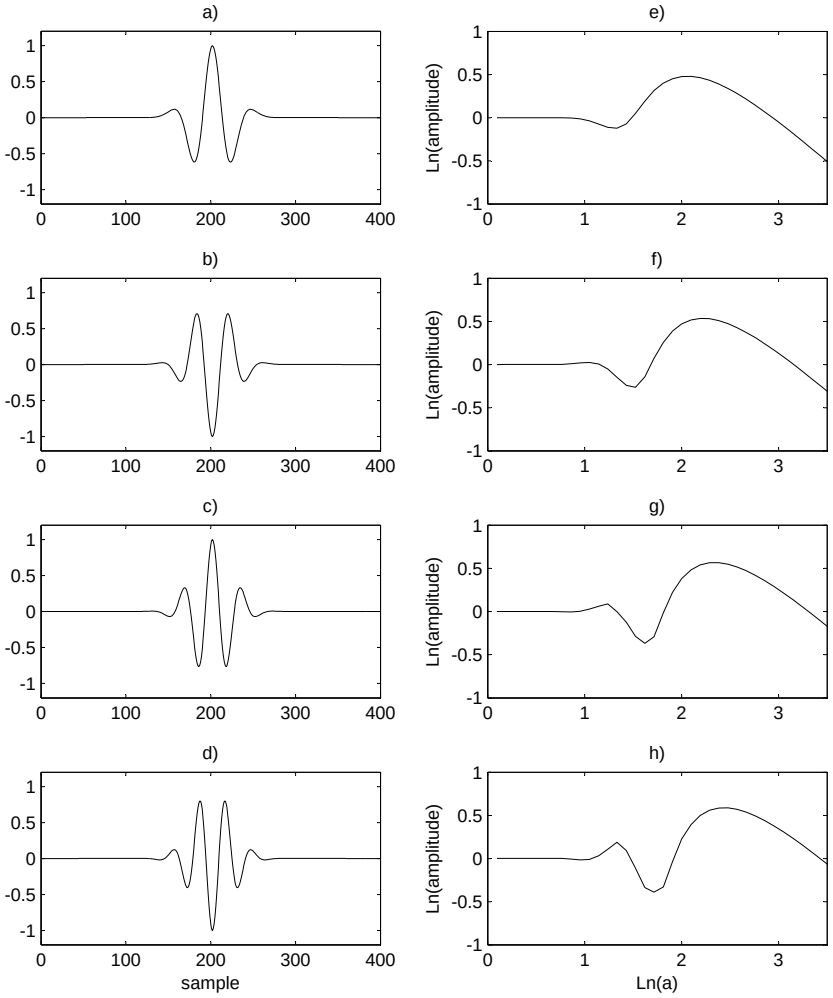

Figure 2. (a-d) Analysing wavelets with derivative orders $n = 4, 6, 8, 10$, respectively. (e-h) Associated ridge functions computed for a window function.

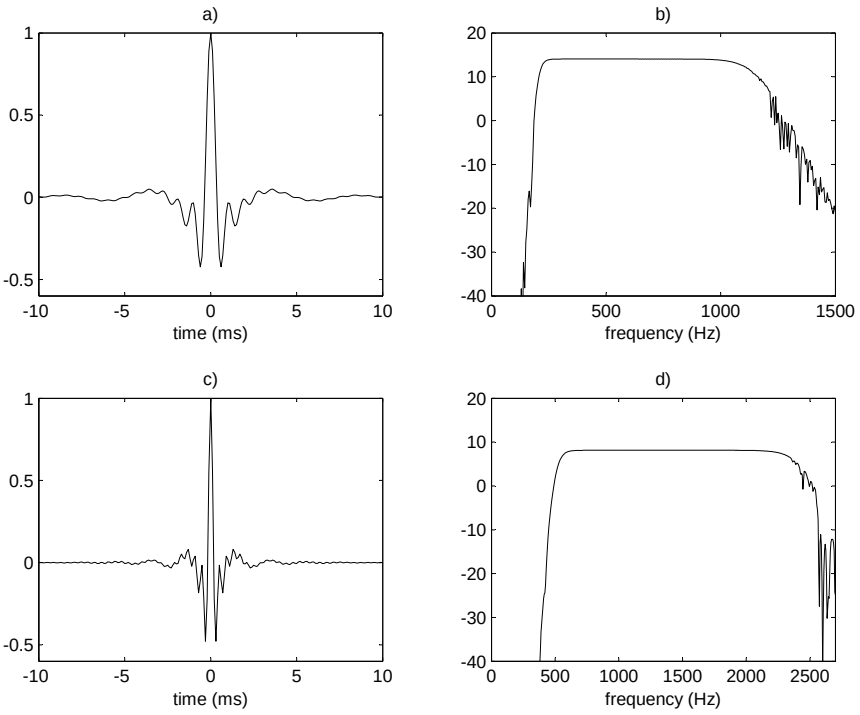

Figure 3. SYSIF seismic sources: The HR (a) and the VHR (b) deconvolved signatures cover the $220-1050Hz$ (b) and $580-2200Hz$ (d) frequency bands, respectively.

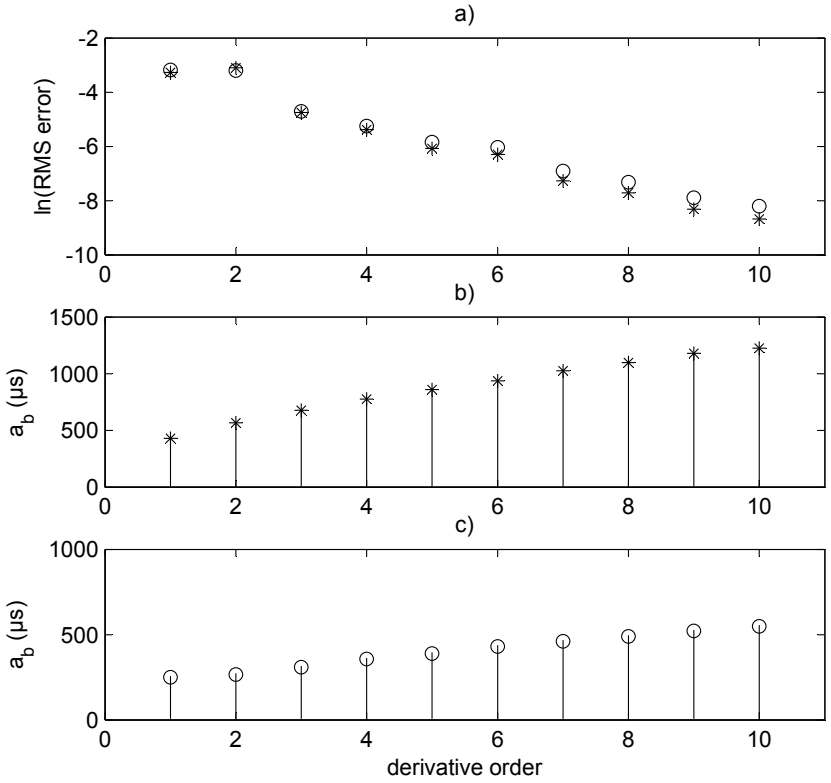

Figure 4. a) Minimum RMS errors versus the derivative order m, for both the SYSIF HR source (stars) and the SYSIF VHR source (circles) and (b,c) the corresponding dilation a_b.

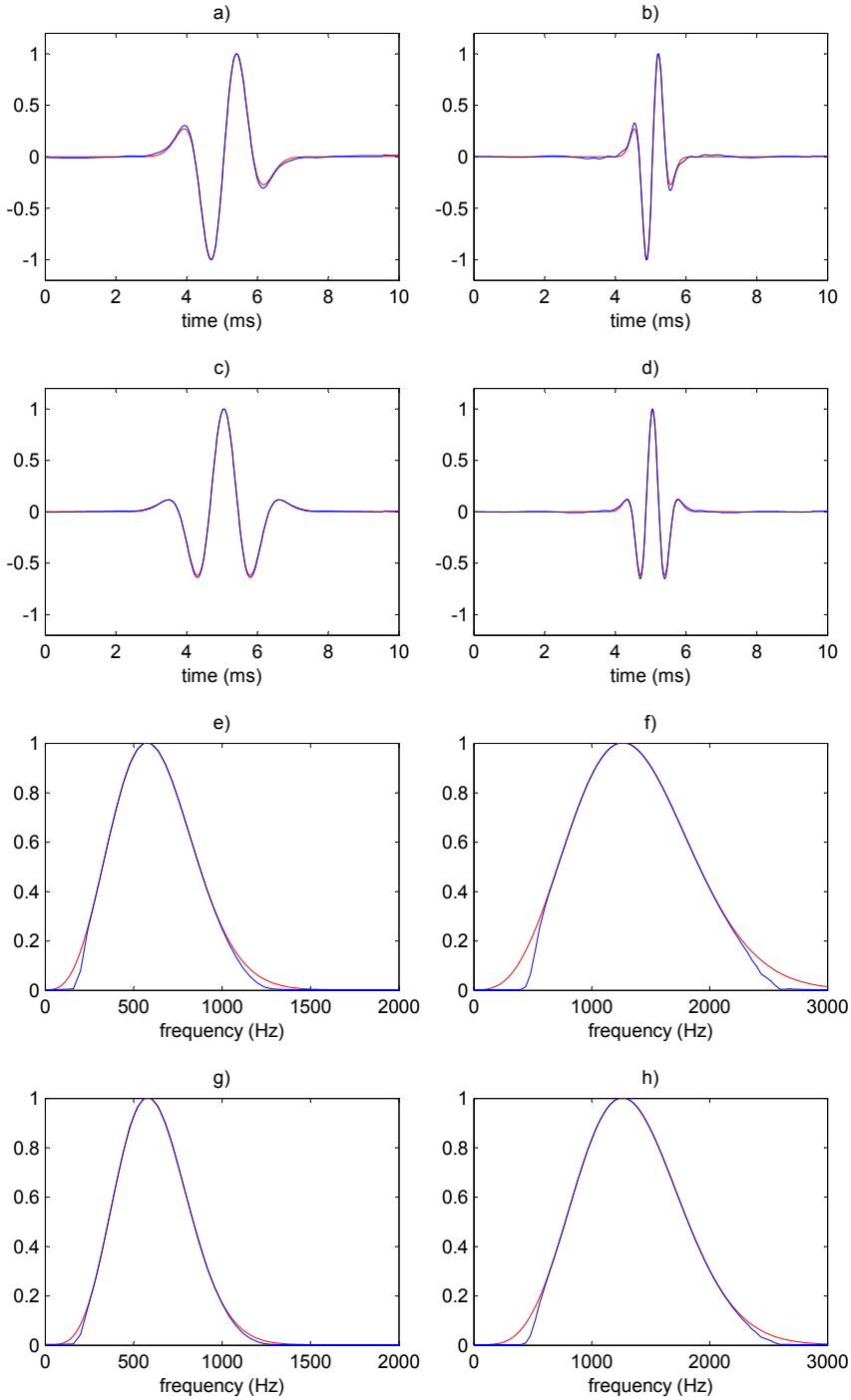

Figure 5. Comparison between $b(t) * s(t)$ (blue) and $b(t)$ (red). In the time domain: (a) HR, $m = 3$; (b) VHR, $m = 3$; (c) HR, $m = 4$; (d) VHR, $m = 4$. In the frequency domain: (e) HR, $m = 3$; (f) VHR, $m = 3$; (g) HR, $m = 4$; (h) VHR, $m = 4$.

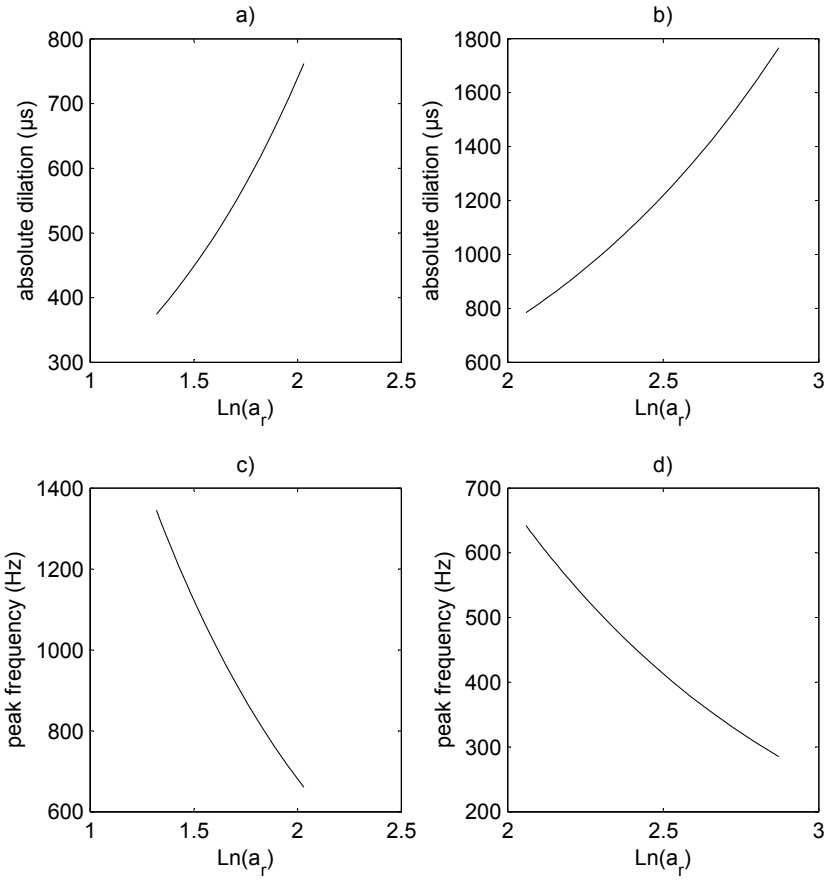

Figure 6. Absolute dilation and peak frequency ranges of the SYSIF HR (on the left) and VHR (on the right) sources, plotted versus the dimensionless dilation $a_r = a/a_0$ for a rms threshold of 20%.

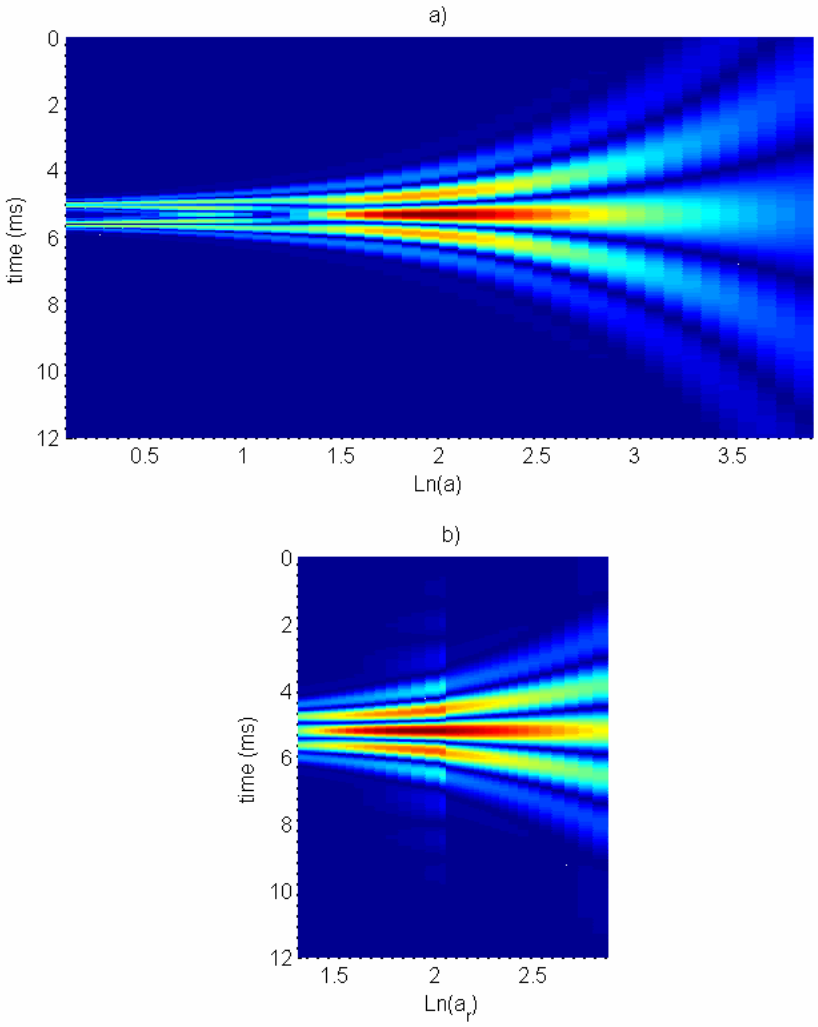

Figure 7. WR of a window function $\Delta z = 45$ cm analysed (a) with the reference wavelet ($n = 5$, $a \in \mathbb{R}^+$), and (b) with the effective wavelet ($l = 5$, $a_r \in \mathcal{R}_{a_r} = \mathcal{R}_{a_r}^{\mathrm{HR}} \cup \mathcal{R}_{a_r}^{\mathrm{VHR}}$) wich takes into account the limited frequency bandwidth of the HR and VHR SYSIF sources.

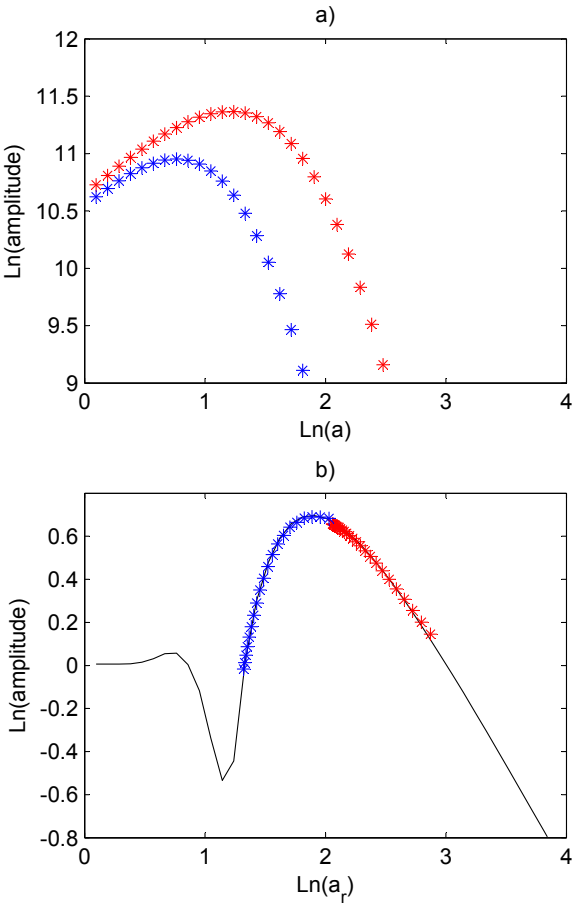

Figure 8. Ridge functions extracted from the SYSIF WR_e ($l = 5$) for a window function $\Delta z = 45\ cm$ (HR in red, VHR in blue, reference ($n = 5$) in solid line): (a) raw version in the reference dilation range and (b) source-corrected version in the effective dilation range ($m = 4$).

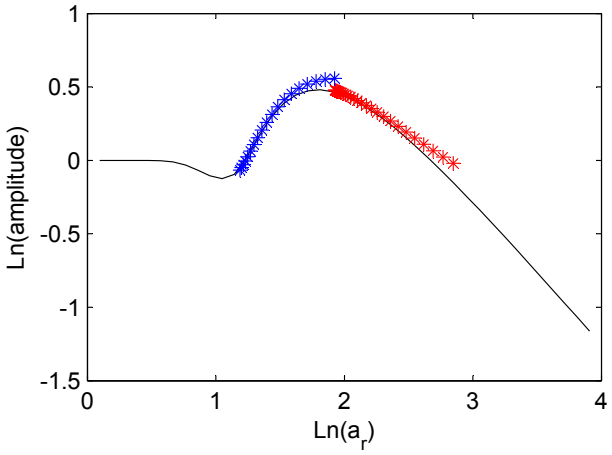

Figure 9. Ridge function extracted from the effective WR_e ($l = 4$) for a window function $\Delta z = 45\ cm$ computed with a source filtering $b(t)$ of the third order ($m = 3$) (HR in red, VHR in blue, reference ($n = 4$) in solid line).

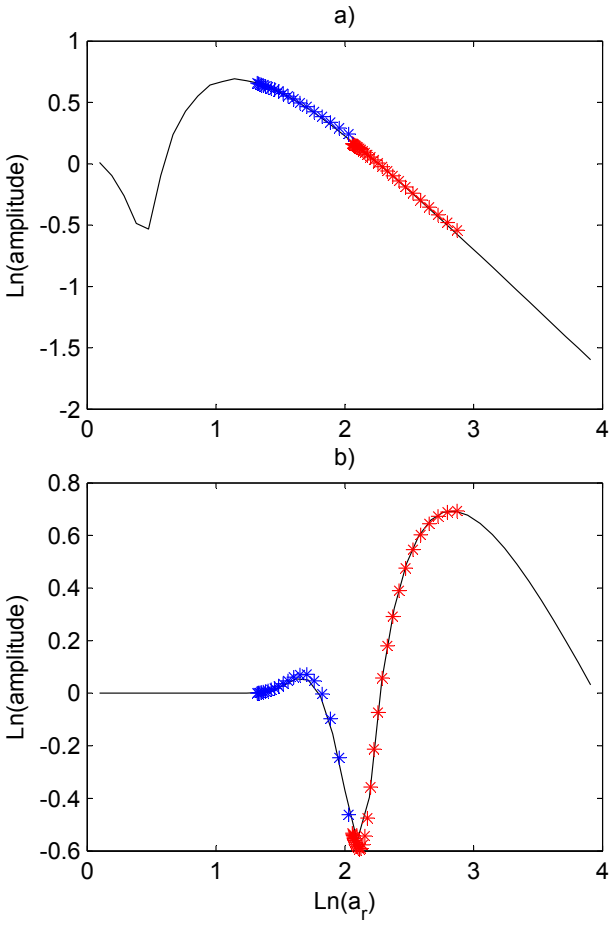

Figure 10. Ridge functions extracted from the SYSIF WR_e ($l = 5$) for window functions of thicknesses (a) $\Delta z = 22\ cm$ and (b) $\Delta z = 112\ cm$ (HR in red, VHR in blue, reference ($n = 5$) in solid line).

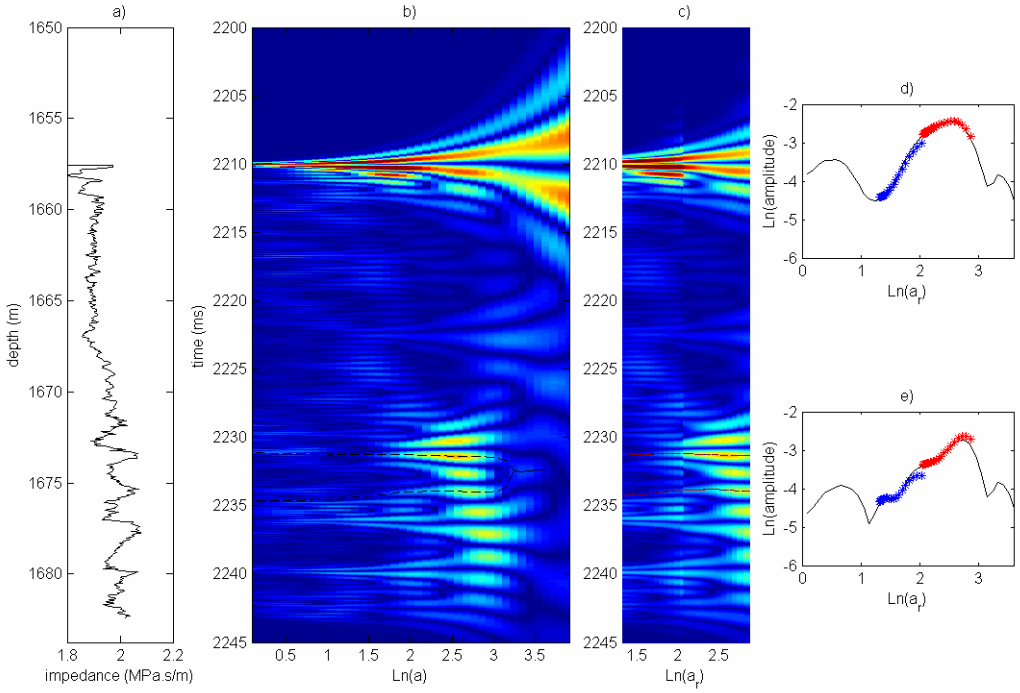

Figure 11. Seismic attributes from the Green's function of hemipelagic sediment impedance (synthetic seismic data): (a) impedance profile, (b) reference WR ($n = 5$, $a \in \mathbb{R}^+$), (c) effective SYSIF WR$_e$ ($l = 5$, $a_r \in \mathcal{R}_{a_r}$) and (d,e) ridge functions of reflectors A and B (WR in solid line and source-corrected WR$_e$ in symbols: HR in red and VHR in blue).

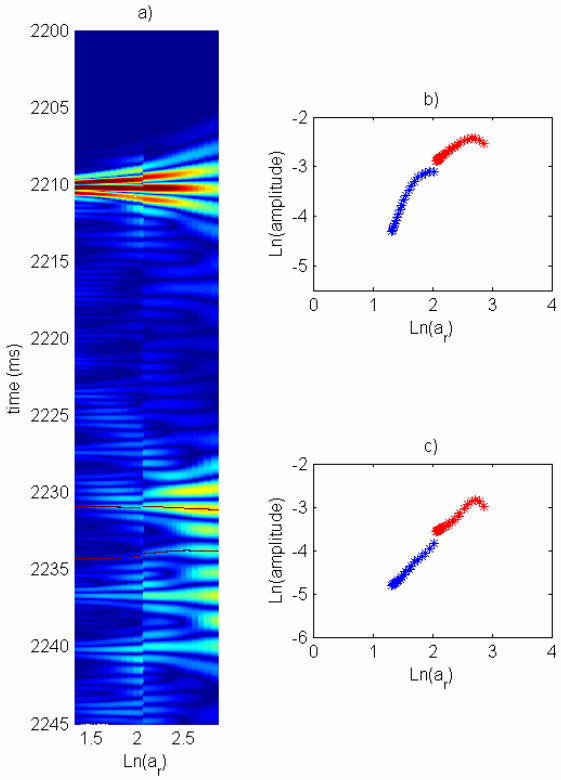

Figure 12. Seismic attributes from field SYSIF data: (a) effective SYSIF WR$_e$ ($l = 5$, $a_r \in \mathcal{R}_{a_r}$) and (b,c) source-corrected ridge functions of reflectors A and B (HR in red and VHR in blue).

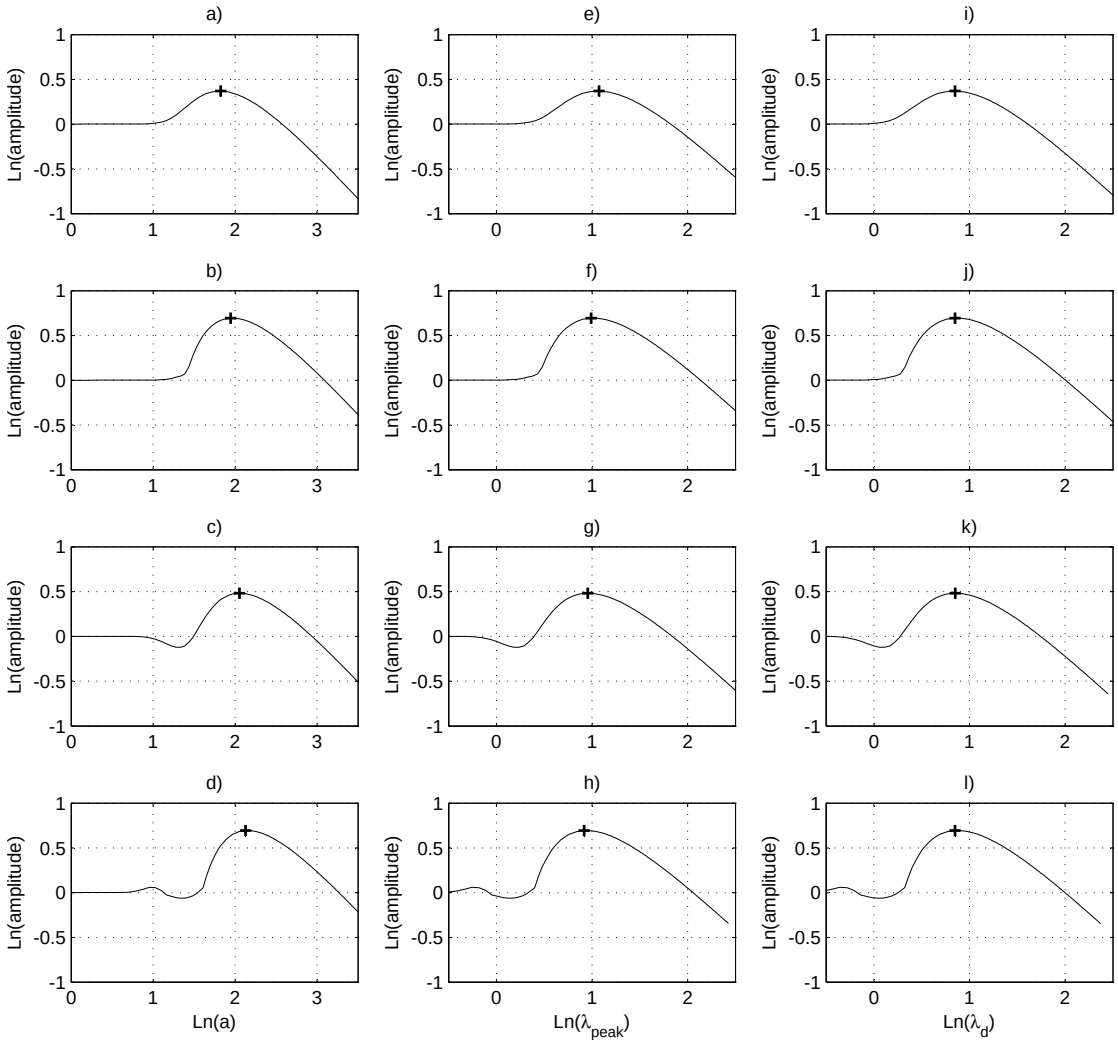

Figure 13. Ridge functions of a window discontinuity analyzed with wavelets of derivative orders $l = 2, 3, 4, 5$ (from top to bottom). The curves are plotted versus the dilation (left), the peak wavelength (middle) and the dominant wavelength (right). Black crosses indicate the location of the maximum: note that for the left and middle columns, this location depends on l whereas it is fixed when the ridge function is plotted versus the dominant wavelength.